Nanoscale Advances

ROYAL SOCIETY OF CHEMISTRY

PAPER

View Article Online
View Journal | View Issue

Cite this: *Nanoscale Adv.*, 2025, **7**, 4919

Synthesis, redox exfoliation, and magnetic nanoparticle decoration of VSe_2 and $SnSe_2$ nanosheets†

Zhengxi Xuan,[ab] Zheng Fu,[ab] B. Medini Rajapakse,[c] Ali Jawaid,[d] Shuo Liu,[af] Richard A. Vaia,*[d] Luis Velarde,*[c] Paras N. Prasad*[ce] and Mark T. Swihart*[abe]

Nanostructures exfoliated from layered van der Waals materials have attracted attention based upon their thickness-dependent optical and electronic properties. While magnetism has been observed in such 2D materials, available approaches to modulate or enhance their magnetic response remain limited. Thus, the magnetic response of 2D materials is of particular interest. Relatively few reports focus on colloidal routes to synthesize layered materials from which 2D nanostructures can be obtained by exfoliation. Herein, we present a general method to synthesize bulk vanadium diselenide (VSe_2) and dual-phase tin diselenide $SnSe_2$–SnSe followed by liquid phase redox exfoliation to delaminate these materials into 2D nanostructures of different thicknesses. The delamination process induces phase changes, affecting the overall magnetic and optical behavior. The magnetization of these 2D nanostructures of different thicknesses increases with an increasing exfoliation degree (decreasing size and thickness). Moreover, we decorated these 2D nanostructures with colloidally synthesized iron oxide dots (Fe_xO_y, ~4 nm diameter). This enhanced the magnetic response, which reached a saturation magnetization of 32 emu g^{-1} for VSe_2–Fe_xO_y and 2.7 emu g^{-1} for $SnSe_2$–Fe_xO_y. A synergistic effect is observed, in which the magnetization of the Fe_xO_y decorated VSe_2 significantly exceeds that of either Fe_xO_y itself or VSe_2 alone. This report provides a general method to synthesize 2D nanostructures of varied thickness and to decorate them with magnetic nanoparticles to achieve synergistic magnetic response.

Received 31st May 2025
Accepted 14th June 2025

DOI: 10.1039/d5na00536a

rsc.li/nanoscale-advances

Introduction

Two-dimensional materials, including transition-metal dichalcogenides (TMDs), graphene, and related structures, feature weak van der Waals (vdW) interactions between their atomically thin layers and strong covalent bonds within the layers. This allows them to be exfoliated into single- or few-layer films with properties that depend upon the number of atomic layers. In recent studies, several synthesis methods have been applied for the preparation of 2D magnetic materials, including the ion exchange method,[1] chemical vapor deposition (CVD)[2] and molecular beam epitaxy.[3] Various 2D materials exhibit strong nonlinear optical properties[4–6] and semiconducting[7,8] properties that make them promising materials for optical sensing[9,10] and energy harvesting.[11–13] Other promising applications for TMDs harness their large surface area and tunable bandgap for oxygen evolution electrocatalysis[14,15] and photodetection.[6,16,17] Some other current research studies explore 2D magnets, including bilayer CrI_3 with a reported Curie temperature (T_c) of 61.5 K[18] and mechanically exfoliated $Cr_2Ge_2Te_6$ with T_c of 66 K.[19]

Most 2D materials have no magnetic ordering due to the absence of magnetic elements or unsaturated bonds.[20] Likewise, modulation of magnetic behavior is difficult in most 2D layered structures. Pristine VSe_2 may exhibit "frustrated intrinsic magnetism",[3] from which ferromagnetic behavior may be introduced by doping[21] or by defects generated during the exfoliation process.[22] Dopants and defects can alter the electronic structure, causing strong interactions between spin impurities. Thus, doping a transition metal into a 2D layered structure can be an effective way to introduce magnetic ordering.[23–26] Substitution of metal atoms within the 2D structure network (MX_2, where M is the metal atom and X is the chalcogen atom) has been shown to induce ferromagnetic

[a]*Department of Chemical and Biological Engineering, University at Buffalo, The State University of New York, Buffalo 14260, NY, USA. E-mail: swihart@buffalo.edu*
[b]*RENEW Institute, University at Buffalo, The State University of New York, Buffalo 14260, NY, USA*
[c]*Department of Chemistry, University at Buffalo, The State University of New York, Buffalo 14260, NY, USA. E-mail: lvelarde@buffalo.edu; pnprasad@buffalo.edu*
[d]*Materials and Manufacturing Directorate, Air Force Research Laboratories, WPAFB, Ohio 45433, USA*
[e]*Institute for Lasers, Photonics, and Biophotonics, The State University of New York, Buffalo 14260, NY, USA*
[f]*The Molecular Foundry, Lawrence Berkeley National Lab, Berkeley, CA 94720, USA*

† Electronic supplementary information (ESI) available. See DOI: https://doi.org/10.1039/d5na00536a

response and enhance coercivity in 2D materials.[25,27,28] For example, an Fe-doped SnSe layered structure exhibited a large coercivity of ~1960 Oe and a Curie temperature (T_c) above room temperature.[26] Non-magnetic doped 2D layered structures have also achieved modulation of coercivity; doping Bi into $SnSe_2$ induced a large coercivity of 4400 Oe.[29]

Here, we report a general colloidal liquid phase method for synthesizing 1T-VSe_2 and 2H-$SnSe_2$ materials, exfoliating these materials, and decorating them with Fe_xO_y nanoparticles to modulate their magnetic response. The 2D bulk materials were synthesized in solution at relatively high temperature (~320 °C) and then processed into thinner layered nanostructures through a redox exfoliation method. In this approach, oxidation of Layered Transition Metal Dichalcogenides (LTMDs), such as MoS_2, generates metal oxide precursors (MOPs) that are adsorbed onto the bulk transition metal dichalcogenide as they are reduced. Highly charged polyoxometalates (POMs) condense onto the bulk material surface and create coulombic repulsion forces that promote material delamination during ultrasonication. Centrifugation at different speeds is then used to size-select less-exfoliated (collected at lower speed and lower RCF) and more-exfoliated (collected at higher speed and higher RCF) fractions. The centrifugal force required to collect a 2D material is a strong function of its surface-to-volume ratio, which increases steeply with the decreasing number of layers. This report demonstrates ultrasonication assisted production of liquid phase exfoliated VSe_2 and $SnSe_2$–SnSe nanosheets. This exfoliation method that delaminated VSe_2 also yielded pure selenium along with VSe_2. In this case, size separation by centrifugation showed that the smallest material (highest RCF) was predominantly pure selenium. Exfoliation of dual phase $SnSe_2$–SnSe yielded mainly $SnSe_2$, but some SnSe phase remained present. The overall crystallinity decreased with increasing RCF (smaller size) but evidence of SnSe persisted. Furthermore, we coupled these 2D layered structures with Fe_xO_y to induce magnetization in the hybrid material. The resulting material exhibited substantial saturation magnetization and coercivity. This work thus demonstrates a general colloidal method to synthesize and exfoliate 2D nanosheets and to integrate the resulting 2D layered structure with Fe_xO_y nanoparticles.

Results and discussion

Scheme 1 and Fig. 1 present the overall process for synthesis and exfoliation of bulk 2D materials reported here. Scheme 1 shows that the transition metal precursor and selenium first dissolve in a high-boiling-point solvent, followed by nucleation and growth of particles at high temperature, forming layered structures. These bulk materials were produced in the stable 2H-$SnSe_2$ and metastable 1T-VSe_2 layered phases, respectively.[30] These materials were the starting point for the exfoliation process illustrated in Fig. 1. Panels (a) and (b) illustrate exfoliation from bulk materials to layered structures of different thicknesses. Panel (c) illustrates decoration of the exfoliated layered structures with Fe_xO_y. In the liquid phase redox exfoliation method (see the Experimental section), the MOPs are reduced to polyoxometalate clusters (POMs) that intercalate between layers and generate repulsive coulombic interactions that drive the material to delaminate into nanostructures of varying thickness. Using different centrifugation speeds allows collection of fractions of more- and less exfoliated material. The remaining ligand on the layer surface assists in Fe_xO_y decoration. In the following discussion, we defined RCF 150 (material collected at a relative centrifugal force of 150) as the thickest layered structure. Likewise, RCF 300 refers to the fraction collected by centrifuging at 300 RCF for 2 hours and so on for RCF 500 and RCF 1000, respectively.

Structural characterization of 2D layered structures

In Fig. 2, panels (a1) (pre-exfoliated VSe_2) to (a5) (VSe_2 RCF 1000–Se) and panels (d1) (pre-exfoliated $SnSe_2$) to (d5) ($SnSe_2$ RCF 1000) show representative TEM images illustrating the size change from pre-exfoliated bulk materials to the thinnest nanostructures. Specifically, we added "–Se" as a suffix to identify VSe_2 samples that were converted to single-phase

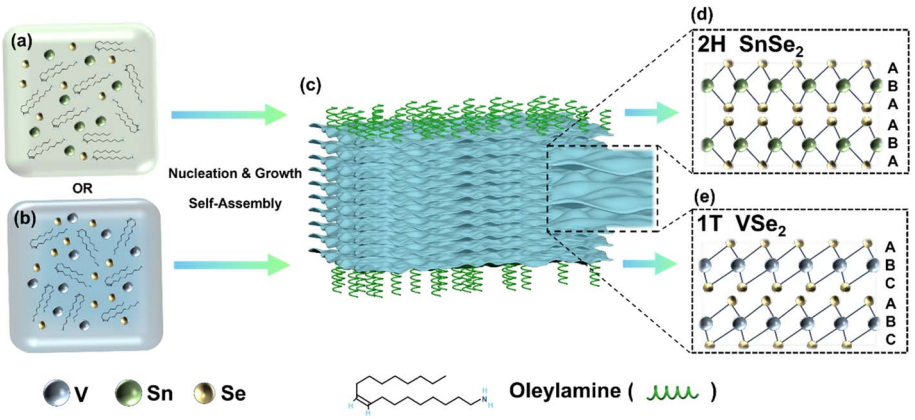

Scheme 1 Solution-phase synthesis of 2D layered nanosheets. (a) $VO(acac)_2$ or (b) $Sn(acac)_2$, along with Se, was dissolved separately in oleylamine, where each reacted individually (in separate experiments) to form (c) bulk nanostructured materials, resulting in (d) 2H-$SnSe_2$ or (e) 1T-VSe_2 nanostructures, respectively.

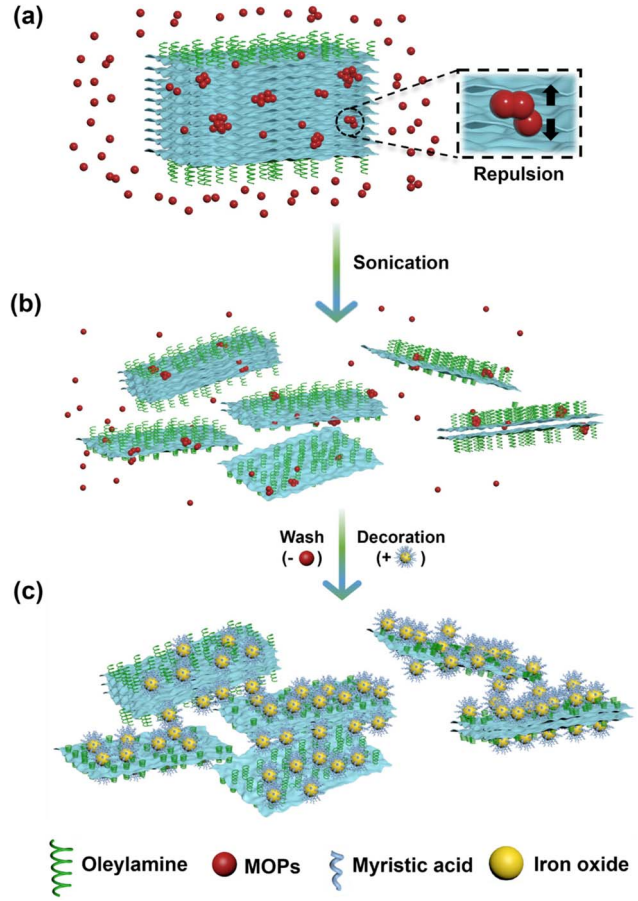

Fig. 1 Mechanism of redox exfoliation of TMDs and their decoration with Fe_xO_y. (a) MOPs (red) assemble into polyoxometalates and adsorb on the bulk material during reduction. (b) Bulk materials are exfoliated to layered nanostructures of varying thickness. (c) Fe_xO_y (yellow) with myristic acid (blue) on their surfaces are coupled with exfoliated nanosheets.

selenium during exfoliation. Overall, increasing exfoliation results in a thickness decrease evident from the contrast difference in the TEM images; the lighter contrast regions correspond to thinner layered structures. The 2D layer thickness was further confirmed by atomic force microscopy (AFM), as shown in Fig. S1 and S2† Non-exfoliated VSe_2 has a relatively large thickness of ~150 nm that decreased to ~20 nm with an increasing degree of exfoliation. Due to the potential aggregation of the layered structures during the sample preparation and drying process as seen in TEM images, we acquired the height profiles for the thinnest portions of each sample. Fig. 2(b) and (e) provide the XRD patterns for MX_2 with different exfoliation levels. Among the VSe_2 samples, a change in the phase occurs during the exfoliation process; pre-exfoliated VSe_2 and VSe_2 RCF 150 exhibit clear peaks corresponding to the 1T-VSe_2 crystal structure. With an increasing degree of exfoliation, however, the VSe_2 RCF 300–Se XRD pattern is dominated by peaks corresponding to elemental Se, and the VSe_2 peaks are nearly gone. VSe_2 RCF 500–Se and VSe_2 RCF 1000–Se exhibit only elemental Se peaks. This suggests that the redox exfoliation process induces partial degradation of the initial 1T-phase VSe_2. We also note that the 1T-phase VSe_2 is thermodynamically metastable,[31] which may be a factor in its degradation. As shown in Fig. 2(c) and S3,† the Raman spectra also indicated a structural transition between VSe_2 RCF 150 to VSe_2 RCF 300–Se consistent with the XRD results. For the thicker samples of layered metal dichalcogenides, the Raman spectrum showed an in-plane E_{2g} peak at 145 cm^{-1} and out-of-plane A_{1g} peak at 230 cm^{-1} confirming the fingerprint of 1T-VSe_2 in non-exfoliated and RCF 150 samples.[22,32] The broad but low intensity peak for all the samples at wavenumbers from 940 cm^{-1} to 990 cm^{-1} may be due to fluorescence. The dominant narrow peak at 520 cm^{-1} observed in all Raman spectra represents the silicon substrate that was also used in AFM measurements.

Similarly, in Fig. 2(e), the XRD pattern also shows a crystallinity change between the dual phase $SnSe_2$–SnSe bulk material to predominantly $SnSe_2$ with a smaller amount of residual SnSe. Panel (d1) shows a TEM image of bulk $SnSe_2$–SnSe with darker contrast and overlapping multiple layered structures. The continuous exfoliation resulted in thinner layered structures (panel (d2)) until single nano-flakes were evident (panel (d5)). These results were also confirmed by AFM (Fig. S2†), from bulk-like $SnSe_2$ with ~600 nm thickness to single nanoflakes with a thickness of ~10 nm. The XRD patterns in Fig. 2(e) show that the pre-exfoliation sample and $SnSe_2$ RCF 150 exhibit peaks corresponding to both $SnSe_2$ and SnSe. The secondary crystal phase, SnSe, is less evident with an increased level of exfoliation, leaving mainly $SnSe_2$ present at RCF 500 (panel (d4)) and RCF 1000 (panel (d5)). In the Raman spectra shown in Fig. 2(f) and S4,† the peaks located at 100 cm^{-1} and 180 cm^{-1} are fingerprints of $SnSe_2$, representing in-plane E_g and out-of-plane vibrational A_{1g} mode, respectively, consistent with previous studies.[33] The Raman signal with sub-peaks at 71 cm^{-1} and 151 cm^{-1} reveals the presence of SnSe.[34] At the same time, two minor or weak Raman peaks were present at 1400 cm^{-1} and 1600 cm^{-1}. These peaks are attributed to the ligands on the nanostructures' surfaces.[35] However, the Raman intensity of the organic groups is negligible compared to that of the metallic peak (Fig. S4c†).

We took advantage of the resulting hydrophobic surface with dilute ligand coverage to attach iron oxide dots (Fe_xO_y) to these materials, inducing a magnetic response. Fig. 3 provides TEM images of Fe_xO_y-decorated VSe_2 and $SnSe_2$–SnSe nanostructures obtained by simple heating of mixed VSe_2 or $SnSe_2$–SnSe with pre-synthesized ligand-coated Fe_xO_y, resulting in ferromagnetic behavior (Fig. 4). Fig. S5† provides HRTEM images that represent Fe_xO_y distributed on the layer surfaces. The size of Fe_xO_y was approximately 4 nm in diameter (Fig. S6a†). Because of their small size, they cannot be definitively identified as Fe_3O_4, γ-Fe_2O_3, or a mixture thereof from the XRD pattern shown in Fig. S6b.† Detailed phase identification is beyond the scope of this work and does not impact our overall conclusions. Fig. S7† shows the physical state of ligand-coated Fe_xO_y, which adhered to the bottom of the vial, indicating that the ligands fully covered the surface of the particles. The FTIR spectrum shows –C–H stretches at 2920 cm^{-1} and 2851 cm^{-1} and C–H scissoring at 1465 cm^{-1} and 1378 cm^{-1} due to the presence of organic ligands on the surface. Fig. S8† shows the physical state of Fe_xO_y

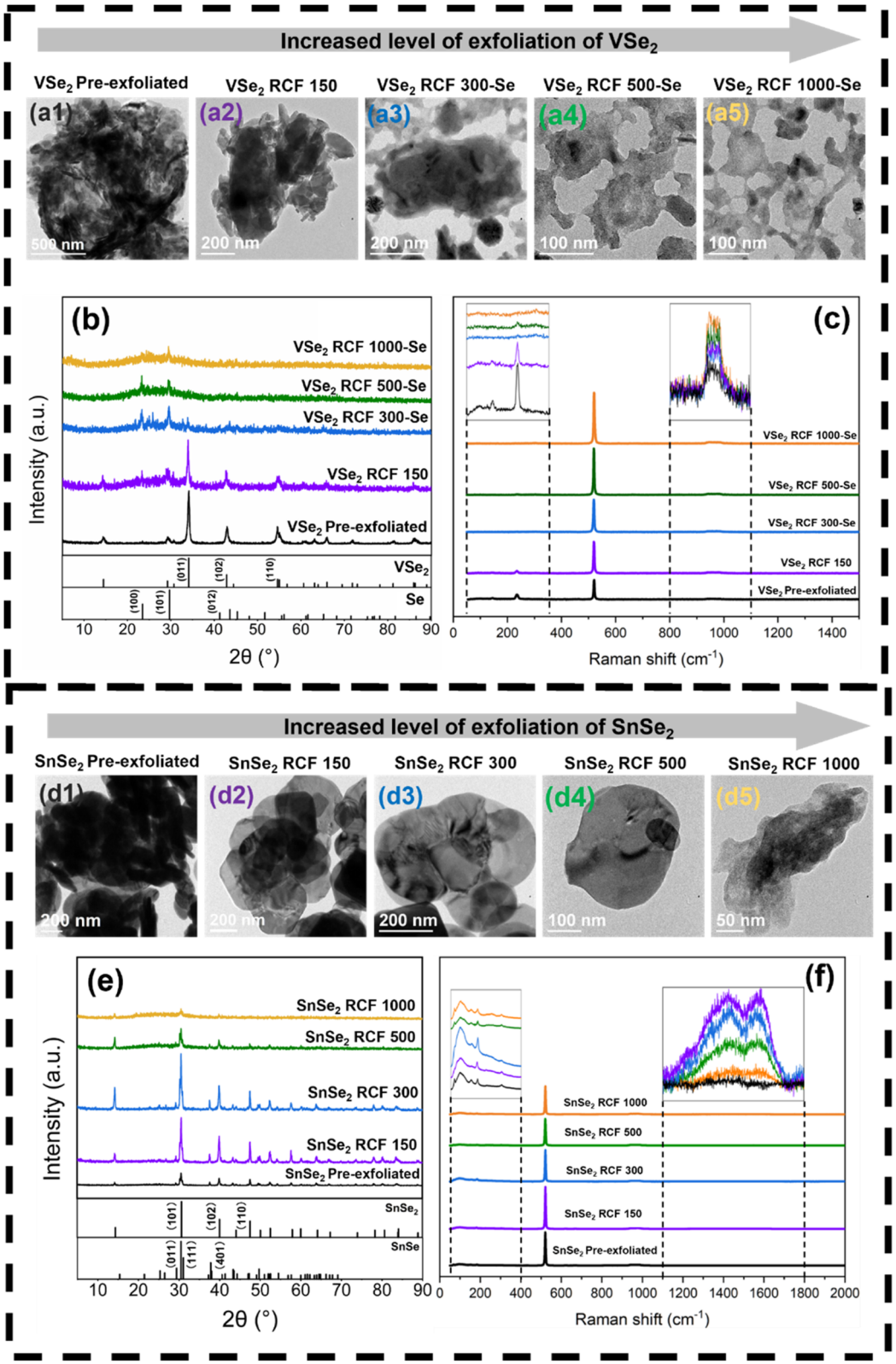

Fig. 2 Characterization of VSe_2 and $SnSe_2$ nanosheets. (a) Panels (a1)–(a5) show representative TEM images for different levels of exfoliation of VSe_2; (b) XRD patterns and (c) Raman spectra for the VSe_2 samples as labeled. (d) Panels (d1)–(d5) provide representative TEM images for different levels of exfoliation of $SnSe_2$; (e) XRD patterns and (f) Raman spectra for $SnSe_2$ samples as labeled.

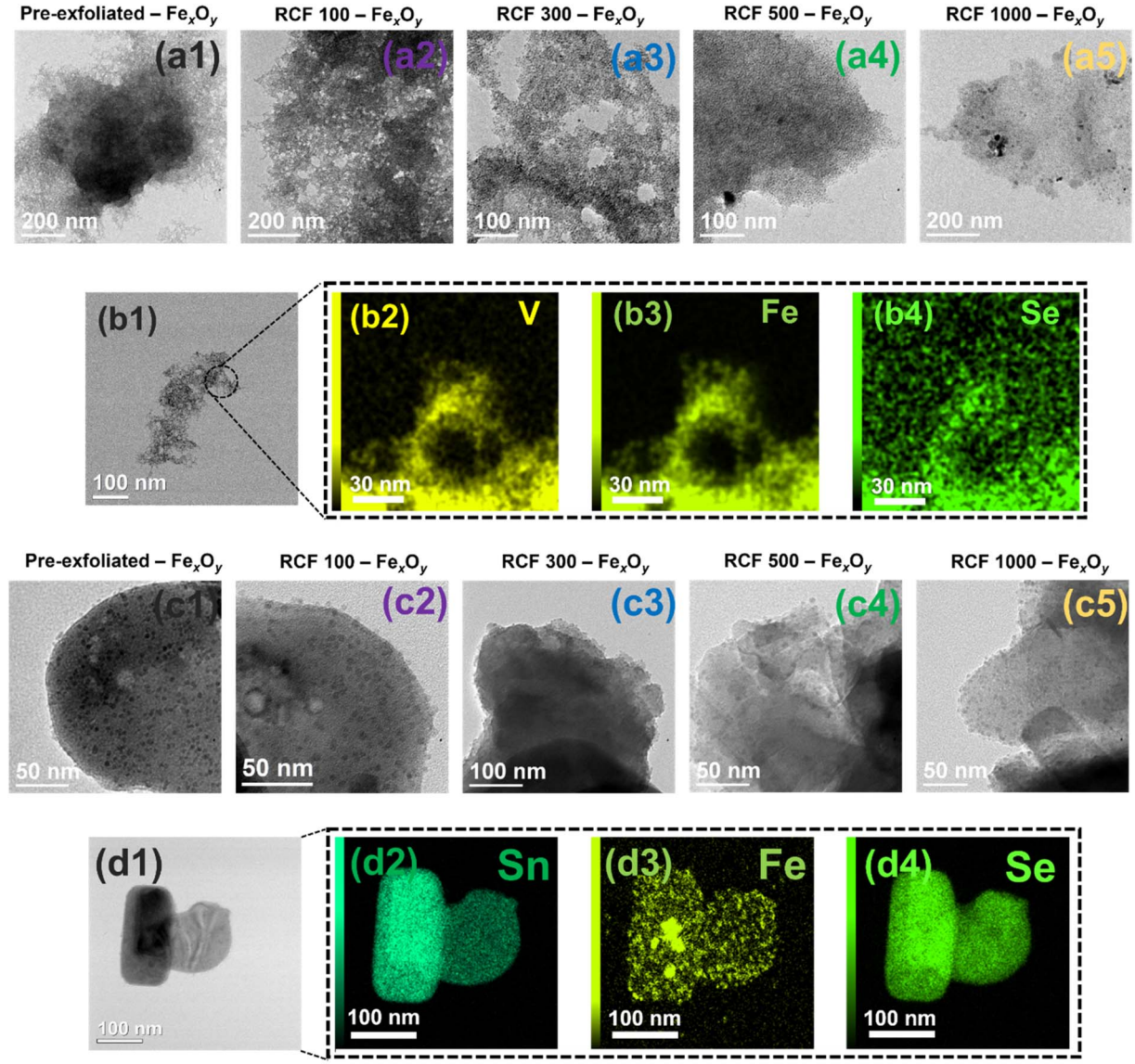

Fig. 3 Characterization of VSe_2 and $SnSe_2$ nanosheets decorated with Fe_xO_y. (a) Panels (a1)–(a5) show representative TEM images of samples with different levels of exfoliation of VSe_2 decorated with Fe_xO_y; (b) panels (b1)–(b4) provide STEM-EDX images of VSe_2 (RCF 150)–Fe_xO_y and corresponding elemental mapping. (c) Panels (c1)–(c5) show TEM images of samples with different levels of exfoliation of $SnSe_2$ decorated with Fe_xO_y; (d) panels (d1)–(d4) show STEM-EDX images of $SnSe_2$ (RCF 150)–Fe_xO_y and corresponding elemental mapping. Inset HRTEM images have a scale bar of 10 nm. Additional zoomed-in TEM images of all nanosheets decorated with Fe_xO_y are shown in Fig. S5.†

nanoparticles prepared without myristic acid, with a typical diameter near 10 nm. The corresponding FTIR spectrum showed weak peaks indicating the presence of relatively little organic material bound to the nanoparticle surface. By comparing these two FTIR spectra, it can be concluded that although oleylamine and myristic acid play a synergetic role in forming quantum dot-sized nanoparticles, myristic acid primarily remains on the surface of Fe_xO_y after synthesis.

The elemental mapping by STEM-EDS shown in Fig. 3, panel (b) and panel (d), confirmed that iron was well dispersed on the VSe_2 and $SnSe_2$–SnSe nanolayer sheets. Although Fe_xO_y were attached to both materials, the Fe_xO_y coverage was lower on the $SnSe_2$–SnSe nanolayer surface compared to the VSe_2 layer surface.

Magnetic characterization of 2D layered structures

The magnetization curves measured for each of these pre-exfoliated and exfoliated samples exhibited a systematic change in the magnetic response. Fig. 4(a) and (b) shows the magnetization curves of the undecorated materials at 8 K; the pre-exfoliated VSe_2 shows paramagnetic behavior with a magnetism of 1 emu g^{-1} at an external magnetic field of 30 kOe. Exfoliated VSe_2 (RCF 150) has a significant increase in magnetization compared with the pre-exfoliated material, showing the highest degree of magnetization among the

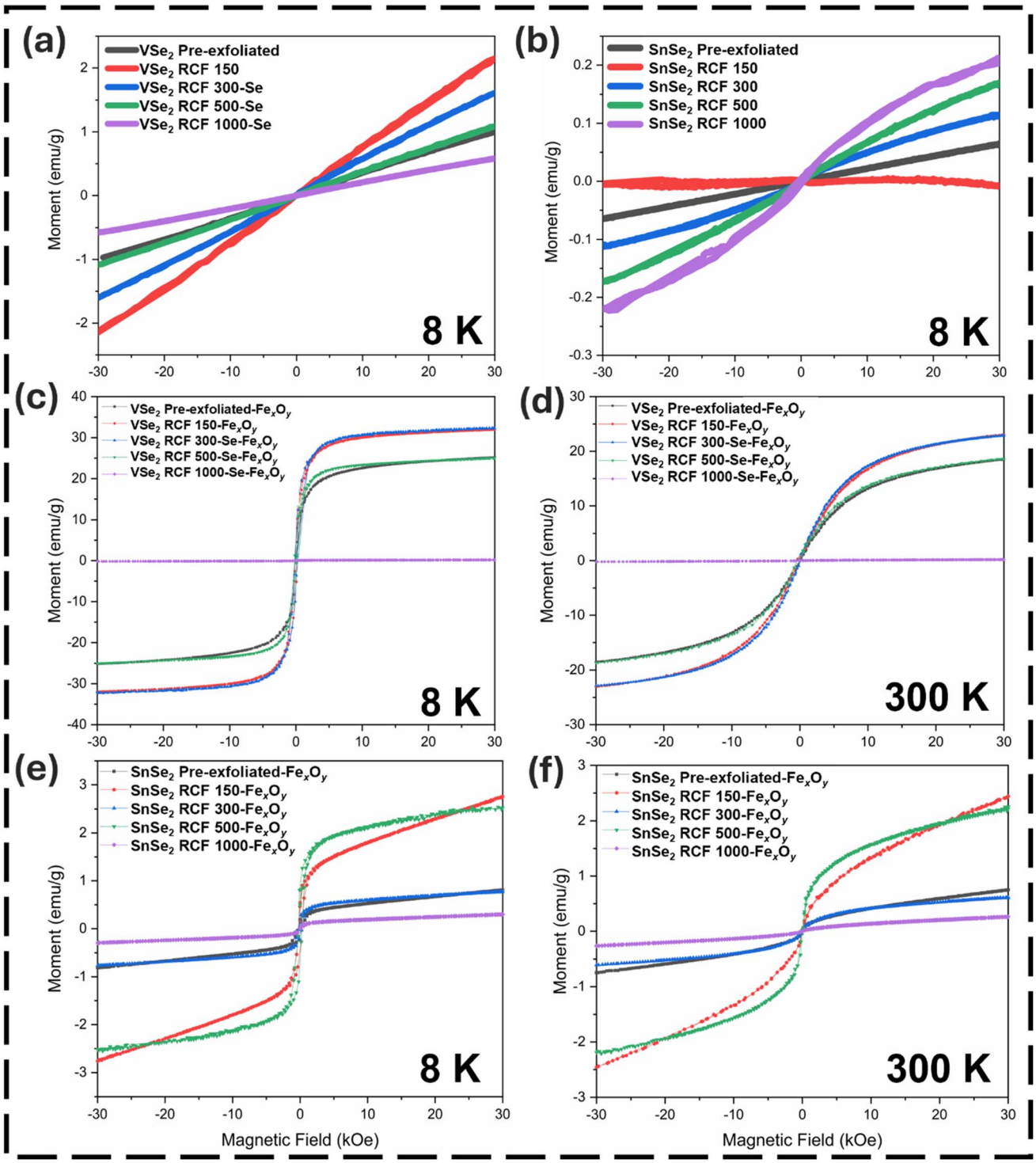

Fig. 4 Magnetization curves for various samples. (a) VSe_2 and (b) $SnSe_2$ measured at 8 K. VSe_2 decorated with Fe_xO_y measured at (c) 8 K and (d) 300 K. $SnSe_2$ decorated with Fe_xO_y measured at (e) 8 K and (f) 300 K.

exfoliated samples, reaching 2.15 emu g^{-1} at 30 kOe. The enhanced magnetism may be related to intrinsic properties of these 2D materials. Mechanical strain generated during the exfoliation process can modulate magnetic properties.[36] Specifically, changes in the V–Se distance may promote accumulation of unpaired electrons around these atoms, thereby enhancing magnetic response.[37]

On further increasing the degree of exfoliation, the magnetization decreased accordingly. VSe_2 RCF 1000–Se, which in fact is mainly elemental selenium, exhibited a magnetization of 0.58 emu g^{-1} at 30 kOe. During the exfoliation process, the thinnest exfoliated VSe_2, which is primarily elemental Se, exhibits a relatively high magnetization of 0.58 emu g^{-1}. This could be attributed to the presence of residual metallic VSe_2, which is

nearly undetectable in the XRD pattern. Additionally, structural defects formed during the liquid-phase exfoliation process may contribute to an enhanced weak magnetic response.[3]

$SnSe_2$, a typical non-magnetic material,[29] exhibits weaker magnetic response compared with VSe_2, but begins to show an "s" shape that arises from magnetization saturation in superparamagnetic materials (Fig. 4(b)). Interestingly, $SnSe_2$ RCF 150 exhibits similar magnetic response compared with bulk $SnSe_2$ but the magnetization increased with the increasing level of exfoliation. $SnSe_2$ RCF 1000, among all these samples, reaches the highest magnetization under an external magnetic field of 30 kOe. During the exfoliation process, magnetism may be altered by the introduction of defects or vacancies, either at Sn or Se sites. These vacancies and defects can modify the local electronic structure and contribute to enhanced magnetic behavior.[3,22] Experimentally, magnetism in 2D layered materials can be induced by extrinsic defects, *e.g.*, Se vacancies can enhance the ferromagnetism of solution-processed VSe_2.[22] Overall, on comparing Fig. 4(a) and (b), $SnSe_2$ alone exhibits much lower magnetization than VSe_2. This is consistent with expected behavior, as undoped $SnSe_2$ is non-magnetic.[29] Multiple theoretical studies predict ferromagnetic behavior in single-layer VSe_2 (ref. 38 and 39) but details of the magnetic response in VSe_2 and its origins are not fully understood.[22] Doping has been reported to induce or enhance magnetic response in both of these materials.[40]

The "s"-shaped magnetization curves for all Fe_xO_y-decorated 2D structures indicating superparamagnetic response associated with Fe_xO_y are shown in Fig. 4(c)–(f).[41] VSe_2 decorated with Fe_xO_y shows a greater increase in saturation magnetization (Fig. 4(c) and (d)) than $SnSe_2$ because Fe_xO_y adhered to it at higher density, as shown in Fig. S5, panels (a1) to (a5),† compared to the magnetization response for $SnSe_2$ decorated with Fe_xO_y (Fig. 4(e) and (f)), with lower Fe_xO_y density (Fig. S5, panels (b1) to (b5)†). Although Fe_xO_y nanoparticles were attached to both materials, the Fe_xO_y coverage was lower on the $SnSe_2$–SnSe surface compared to the VSe_2 surface. These findings are consistent with the EDX elemental mapping, which confirms the uniform distribution of iron on both nanostructures. (Fig. 3, panel (b) and panel (d)). However, pure Fe_xO_y only exhibited a saturation magnetization of around 13 emu g^{-1} at 8 K (Fig. S9†), which is far less than that of VSe_2 decorated with Fe_xO_y, 32 emu g^{-1} at 8 K. The low magnetic response of pure Fe_xO_y can be attributed to its small size and ligand coverage that creates a magnetically inactive surface layer that occupies a significant fraction of the particle volume.[42,43] The decoration of Fe_xO_y on the nanolayer surface may assist the removal of the ligand during coupling. The heating temperature used for coupling is high enough to drive some ligand desorption, allowing Fe_xO_y to make close contact with the layered material. This close coupling results in higher magnetization in nanolayer VSe_2 decorated with Fe_xO_y than in pure Fe_xO_y. The enhancement of the magnetic signal of the decorated nanosheets is not only attributed to the coverage of iron oxide nanoparticles, but also arises from magnetic dipole interaction modulation between iron oxide and the layered nanostructures.[44]

During the exfoliation process, larger particles are reduced to much thinner 2D layered structures, which possess a larger surface area. Thinner nanostructures collected at higher RCF thus increase the Fe_xO_y : MX_2 ratio per hybrid particle, resulting in a larger magnetic response during the decoration process. For example, exfoliated samples of VSe_2 decorated with Fe_xO_y generally exhibit higher magnetic responses than those with lower level of exfoliation (Fig. 4(c) and (d)). This may also apply to the non-metallic VSe_2 RCF 300–Se sample decorated with iron oxide, which shows a similar magnetic response to VSe_2 RCF 150 decorated with iron oxide due to its higher surface area. For the Fe_xO_y-decorated RCF 1000 sample from VSe_2 (actually Se) we could not measure any magnetization. This was unexpected, because in the TEM images, Fe_xO_y are visible on the layered material. This may simply be due to small sample size and higher organic content in this smallest size fraction.

As shown in Fig. 4(e) and S10,† the Fe_xO_y-decorated $SnSe_2$ RCF 500 exhibited the largest coercivity at 8 K, at about 0.22 kOe, and the sharpest "s"-shaped response among the $SnSe_2$ samples decorated with Fe_xO_y. However, $SnSe_2$ coupled with Fe_xO_y reached only 2.8 emu g^{-1} maximum magnetization measured at 8 K, which is far less than that of VSe_2 coupled with Fe_xO_y or even pure Fe_xO_y. Also, among the samples of $SnSe_2$ coupled with Fe_xO_y, although $SnSe_2$ RCF 500–Fe_xO_y exhibited the highest coercivity and sharpest "s" shape, $SnSe_2$ RCF 150–Fe_xO_y exhibited higher magnetization at fields above 21 kOe. Similar to VSe_2 RCF 1000–Fe_xO_y, $SnSe_2$ RCF 1000–Fe_xO_y exhibits minimal magnetic response. Compared to other doped magnetic semiconductors, doped $SnSe_2$ exhibits a coexistence of ferromagnetic and antiferromagnetic interactions, resulting in unsaturated magnetization even under a 30 kOe magnetic field.[40]

Overall, comparing the *M*–*H* (Fig. 4) and *M*–*T* (Fig. S11†) curves for all samples, including undecorated layered nanostructures, magnetic Fe_xO_y decorated nanostructures and pure Fe_xO_y nanoparticles (Fig. S9 and S12†), showed that the magnetic signal in the decorated samples is mainly attributable to the magnetic Fe_xO_y nanoparticles. The decorated layered nanostructures exhibit the same temperature dependence as pure iron oxide, but higher overall magnetization. Thus, coupling with VSe_2 amplifies, but does not fundamentally alter, the magnetization behavior. This observation provides valuable insight into the role of 2D layered nanostructures in altering interactions among the Fe_xO_y nanoparticles. Amplified magnetization was only observed when Fe_xO_y particles were coupled to/through VSe_2 and not when they were in even closer contact with one another (as a dried powder) alone or when they were coupled to/through $SnSe_2$. This suggests that not only the high surface area but also the electronic structure of the 2D material is important. These sites enable the coupling of uniform and stable colloidal nanostructures, further enhancing their potential for a wide range of applications.

Conclusion

In summary, we have developed a general route combining a colloidal synthesis and redox exfoliation method to produce metal dichalcogenide nanosheets. These were then coupled to

pre-synthesized Fe_xO_y by simple heating to desorb sufficient ligands to allow Fe_xO_y to make close contact with the 2D material. We studied the magnetic and optical properties of these structures after fractionation into samples of different exfoliation levels by centrifugation at different speeds. The phase and composition of VSe_2 changed with decreasing size (increasing RCF in centrifugation) until metallic Se remained. In contrast, $SnSe_2$–SnSe mainly showed a decrease in crystallinity in exfoliated samples of smaller size. Magnetic coupling of Fe_xO_y to the VSe_2 fractions generated a higher magnetization response than iron oxide alone, reflecting the effect of coupling of Fe_xO_y to the VSe_2 layers. The $SnSe_2$ decorated with Fe_xO_y did not exhibit enhanced magnetization but exhibited higher coercivity than Fe_xO_y alone. This study suggests more general potential for 2D materials synthesized by colloidal synthesis and redox exfoliation to be decorated with pre-synthesized nanoparticles, which could be plasmonic nanoparticles or quantum dots as well as superparamagnetic iron oxide, opening up new avenues for exploring interaction between 0D and 2D materials.

Experimental section

Chemicals and materials

Vanadyl(IV) acetylacetonate ($VO(acac)_2$, 99%), iron(III) acetylacetonate ($Fe(acac)_3$, 99+%) selenium (Se, 99+%), cumyl hydroperoxide, 80% and hydroquinone, 99.5% were purchased from Acros Organics. Tin(II) acetylacetonate ($Sn(acac)_2$, min. 98%) was purchased from Strem Chemicals. Molybdenum(IV) sulfide (99%, metals basis) and 1-octadecene (ODE, 90%) were purchased from Alfa Aesar. Acetonitrile (99.9%, extra dry over molecular sieve) was purchased from Thermo Scientific. All chemicals were used as received without further purification.

Pre-treatment of MoS_2 to generate molecular metal oxide precursors (MOPs)

MoS_2 was pre-cleaned by refluxing in ethanol/acetone(1 : 1) for 24 hours, followed by vacuum filtration to remove surface impurities. Pre-cleaned MoS_2 was then oxidized to MOPs by dispersing 32 mg MoS_2 per 1 mL acetonitrile followed by adding 12 μL cumene hydroperoxide per 1 mL MoS_2 dispersion and stirring in a three-neck flask at 40 °C for 24 hours. The light-yellow colored supernatant containing MOPs was obtained by centrifuging the resulting products at 5000 RCF for 10 min to remove remaining MoS_2.

Synthesis of VSe_2 and $SnSe_2$

$SnSe_2$–SnSe and VSe_2 were synthesized based on a previously reported method.[21] In summary, to prepare VSe_2, 2 mmol of $VO(acac)_2$, 4 mmol Se and 30 mL OAm were added to a three-neck flask. To prepare $SnSe_2$–SnSe, 1 mmol of $Sn(acac)_2$ and 2 mmol Se mixed with 15 mL OAm were added to a three-neck flask. In each case, the mixture was heated to 110 °C under argon flow for 30 min to remove oxygen. Then the flask was wrapped with glass wool to minimize heat loss during the reaction. The mixture was heated at a rate of 4.5 °C min^{-1} to 300 °C and then heated at a rate of 1.5 °C min^{-1} 320 °C. Then the mixture was held at 320 °C for about 30 min. The reaction product was removed from the heating mantle and allowed to cool to room temperature. The product was collected by centrifugation. Samples were washed with ethanol and hexane three times and centrifuged at 8000 rpm to further remove unreacted precursors and ligands.

Synthesis of Fe_xO_y nanoparticles

One mmol of $Fe(acac)_3$, 0.88 mmol myristic acid, and 1 mL OAm and 18 mL ODE were added to a three-neck flask. The mixture was heated to 110 °C under argon flow for 30 min to remove oxygen. Then the flask was wrapped with glass wool to minimize heat loss during the reaction and further heated to 280 °C for 60 min at rate of 2.8 °C min^{-1}. The product nanoparticles were collected by centrifugation after cooling to room temperature. The product was collected and washed with ethanol and toluene three times and centrifuged at 10 000 rpm to further remove unreacted precursors and ligands. The final product was dispersed in 10 mL of toluene for further use.

VSe_2 and $SnSe_2$–SnSe exfoliation

Exfoliation of layered metal dichalcogenides. Pre-synthesized VSe_2 or $SnSe_2$ was dispersed in acetonitrile containing MOPs (0.2 M) and mixed in a three-neck flask under vigorous stirring for 24 hours. Then hydroquinone (5 μmol mL^{-1}) was added, followed by bath sonication for 72 hours to initiate exfoliation. The product mixture was centrifuged at 8000 RCF for 15 min to separate solids from unreacted chemicals. The collected solids were washed with acetonitrile twice, each time collected by centrifugation at 8000 RCF for 10 min. The cleaned bulk material was then centrifuged at different speeds to separate fractions of different sizes and thicknesses; the bulk material was initially centrifuged at 150 RCF for 2 h to remove the largest, thickest material. The remaining supernatant was then centrifuged at 300 RCF to separate the next smaller fraction, and the process continued, by centrifuging the supernatant at 500 RCF for 2 hours and 1000 RCF for 3 hours to obtain the smaller size fractions. The collected materials were redispersed in acetonitrile for further characterization and use.

Coupling Fe_xO_y with metal dichalcogenides. Each aliquot of TMD was mixed with an excess of Fe_xO_y and 10 mL of ODE in a three-neck flask. The mixture was heated to 120 °C under flowing argon with vigorous stirring, allowing removal of low boiling solvents including toluene and acetonitrile. The mixture was further heated to 200 °C at a rate of 2.3 °C min^{-1} and held at 200 °C for about 20 min before being removed from the heating mantle and allowed to cool to room temperature. It was then collected and washed with ethanol and toluene three times, in each case centrifuging at 8000 rpm. To separate the Fe_xO_y-decorated metal dichalcogenide from unreacted Fe_xO_y, we centrifuged each sample at the same RCF used to collect that fraction of the layered material. Fig. S13† shows examples of the product before this additional washing step. Without this additional washing step, unbound Fe_xO_y remained in the product, which would affect the magnetization measurements.

Characterization

TEM images were acquired using a JEOL JEM 2010 microscope at 200 kV. STEM-EDX images were acquired using a JEOL F200 cold field emission TEM/STEM at 200 kV, with dual 100 nm SDD EDX detectors and a OneView IS CMOS camera for *in situ*/*operando* imaging at high speeds by STEMx 4D STEM. XRD patterns were acquired using a Rigaku Ultima IV diffractometer with a Cu Kα X-ray source. Magnetization hysteresis loops were obtained using a Physical Property Measurement System (PPMS) – Quantum Design Evercool II. Atomic force microscopy height images were recorded using an OmegaScope-R scanning probe microscope (AIST-NT Inc.) with silicon AFM probes ($k_n \sim$ 42 N m^{-1}, TESPA-V2, BRUKER) in tapping mode at 0.2 Hz scanning speed. Images were processed using Gwyddion software. Micro Raman experiments were carried out with a Horiba LabRAM HR confocal Raman spectrometer with a 532 nm excitation wavelength, 600 grooves per mm grating, 100× LWD objective (NA = 0.90) and a thermoelectrically cooled CCD detector (Synapse, HORIBA scientific). Incident laser power was kept at 0.37 mW for all measurements. Each spectrum was obtained by averaging 10 acquisitions over 10 s.

Data availability

The data supporting this article have been included as part of the ESI.†

Conflicts of interest

There are no conflicts to declare.

Acknowledgements

The authors acknowledge support from the Air Force Office of Scientific Research (Program Officer: Dr Brett Pokines), Grant # FA9550-20-1-0428. STEM-EDX measurements were performed by Kevin Mcllwrath from JEOL, using a TEM at the University of Pennsylvania, courtesy of Eric Stack/Doug Yates.

References

1 H. Yang, F. Wang, H. Zhang, L. Guo, L. Hu, L. Wang, D.-J. Xue and X. Xu, *J. Am. Chem. Soc.*, 2020, **142**, 4438–4444.
2 J. Jang, P. K. Srivastava, M. Joe, S.-G. Jung, T. Park, Y. Kim and C. Lee, *ACS Nano*, 2024, **19**, 999–1006.
3 R. Chua, J. Yang, X. He, X. Yu, W. Yu, F. Bussolotti, P. K. J. Wong, K. P. Loh, M. B. Breese and K. E. J. Goh, *Adv. Mater.*, 2020, **32**, 2000693.
4 Q. Guo, X.-Z. Qi, L. Zhang, M. Gao, S. Hu, W. Zhou, W. Zang, X. Zhao, J. Wang and B. Yan, *Nature*, 2023, **613**, 53–59.
5 S. Yu, X. Wu, Y. Wang, X. Guo and L. Tong, *Adv. Mater.*, 2017, **29**, 1606128.
6 F. Zhou, I. Abdelwahab, K. Leng, K. P. Loh and W. Ji, *Adv. Mater.*, 2019, **31**, 1904155.
7 D. Kim, H. J. Jung, I. J. Park, B. W. Larson, S. P. Dunfield, C. Xiao, J. Kim, J. Tong, P. Boonmongkolras and S. G. Ji, *Science*, 2020, **368**, 155–160.
8 Y. Yang, S. C. Liu, X. Wang, Z. Li, Y. Zhang, G. Zhang, D. J. Xue and J. S. Hu, *Adv. Funct. Mater.*, 2019, **29**, 1900411.
9 J. Ping, Z. Fan, M. Sindoro, Y. Ying and H. Zhang, *Adv. Funct. Mater.*, 2017, **27**, 1605817.
10 Z. L. Lei and B. Guo, *Adv. Sci.*, 2022, **9**, 2102924.
11 S. A. Han, J. Lee, J. Lin, S.-W. Kim and J. H. Kim, *Nano Energy*, 2019, **57**, 680–691.
12 H. Cai, Y. Guo, H. Gao and W. Guo, *Nano Energy*, 2019, **56**, 33–39.
13 R. Yang, R. Xu, W. Dou, M. Benner, Q. Zhang and J. Liu, *Nano Energy*, 2021, **83**, 105849.
14 Z. Fang, L. Peng, H. Lv, Y. Zhu, C. Yan, S. Wang, P. Kalyani, X. Wu and G. Yu, *ACS Nano*, 2017, **11**, 9550–9557.
15 X. Cao, Y. Hong, N. Zhang, Q. Chen, J. Masud, M. A. Zaeem and M. Nath, *ACS Catal.*, 2018, **8**, 8273–8289.
16 X. Zhou, L. Gan, W. Tian, Q. Zhang, S. Jin, H. Li, Y. Bando, D. Golberg and T. Zhai, *Adv. Mater.*, 2015, **27**, 8035–8041.
17 N. Huo and G. Konstantatos, *Adv. Mater.*, 2018, **30**, 1801164.
18 S. Jiang, J. Shan and K. F. Mak, *Nat. Mater.*, 2018, **17**, 406–410.
19 C. Gong, L. Li, Z. Li, H. Ji, A. Stern, Y. Xia, T. Cao, W. Bao, C. Wang and Y. Wang, *Nature*, 2017, **546**, 265–269.
20 Z. Zhao, W. Li, Y. Zeng, X. Huang, C. Yun, B. Zhang and Y. Hou, *Small Struct.*, 2021, **2**, 2100077.
21 L.-Y. Hu, L.-F. Yu, H. Yang, X. Xu, F. Wang and X.-H. Xu, *Rare Met.*, 2021, **40**, 2501–2507.
22 W. Yu, J. Li, T. S. Herng, Z. Wang, X. Zhao, X. Chi, W. Fu, I. Abdelwahab, J. Zhou and J. Dan, *Adv. Mater.*, 2019, **31**, 1903779.
23 F. Yang, P. Hu, F. F. Yang, B. Chen, F. Yin, R. Sun, K. Hao, F. Zhu, K. Wang and Z. Yin, *Adv. Sci.*, 2023, 2300952.
24 S. J. Yun, D. L. Duong, D. M. Ha, K. Singh, T. L. Phan, W. Choi, Y. M. Kim and Y. H. Lee, *Adv. Sci.*, 2020, **7**, 1903076.
25 D. Shen, B. Zhao, Z. Zhang, H. Zhang, X. Yang, Z. Huang, B. Li, R. Song, Y. Jin and R. Wu, *ACS Nano*, 2022, **16**, 10623–10631.
26 G. Mei, W. Tan, X. Cui, C. Wang, Q. Yuan, Y. Li, C. Lou, X. Hou, M. Zhao, Y. Liu, W. Ji, X. Zhang, M. Feng and L. Cao, *Mater. Today Phys.*, 2023, **38**, 101251.
27 S. Ahmed, X. Ding, P. P. Murmu, N. Bao, R. Liu, J. Kennedy, L. Wang, J. Ding, T. Wu and A. Vinu, *Small*, 2020, **16**, 1903173.
28 M. Habib, Z. Muhammad, R. Khan, C. Wu, Z. Ur Rehman, Y. Zhou, H. Liu and L. Song, *Nanotechnology*, 2018, **29**, 115701.
29 J.-h. Luo, B. Li, J.-m. Zhang, M.-z. Zhong, Q.-l. Xia, Y.-z. Nie and G.-h. Guo, *J. Magn. Magn. Mater.*, 2019, **486**, 165269.
30 S. Chae, S. S. Chae, M. Choi, H. min Park, H. Chang, J.-O. Lee and T. I. Lee, *Nano Energy*, 2019, **56**, 65–73.
31 D. Li, X. Wang, C.-m. Kan, D. He, Z. Li, Q. Hao, H. Zhao, C. Wu, C. Jin and X. Cui, *ACS Appl. Mater. Interfaces*, 2020, **12**, 25143–25149.

32 J. Feng, R. A. Susilo, B. Lin, W. Deng, Y. Wang, B. Li, K. Jiang, Z. Chen, X. Xing and Z. Shi, *Adv. Electron. Mater.*, 2020, **6**, 1901427.
33 Y. Zhang, Y. Shi, M. Wu, K. Zhang, B. Man and M. Liu, *Nanomaterials*, 2018, **8**, 515.
34 F. Li, H. Wang, R. Huang, W. Chen and H. Zhang, *Adv. Funct. Mater.*, 2022, **32**, 2200516.
35 Y. El Mendili, F. Grasset, N. Randrianantoandro, N. Nerambourg, J.-M. Greneche and J.-F. o. Bardeau, *J. Phys. Chem. C*, 2015, **119**, 10662–10668.
36 W. Ci, H. Yang, W. Xue, R. Yang, B. Lv, P. Wang, R.-W. Li and X.-H. Xu, *Nano Res.*, 2022, **15**, 7597–7603.
37 M. Bonilla, S. Kolekar, Y. Ma, H. C. Diaz, V. Kalappattil, R. Das, T. Eggers, H. R. Gutierrez, M.-H. Phan and M. Batzill, *Nat. Nanotechnol.*, 2018, **13**, 289–293.
38 Y. Ma, Y. Dai, M. Guo, C. Niu, Y. Zhu and B. Huang, *ACS Nano*, 2012, **6**, 1695–1701.
39 F. Li, K. Tu and Z. Chen, *J. Phys. Chem. C*, 2014, **118**, 21264–21274.
40 H. Huang, A. Rahman, J. Wang, Y. Lu, R. Akiyama and S. Hasegawa, *J. Appl. Phys.*, 2021, **130**, 223903.
41 G. Villalpando, A. M. Ferrenti, R. Singha, X. Song, G. Cheng, N. Yao and L. M. Schoop, *ACS Nano*, 2022, **16**, 13814–13820.
42 L. Qiao, Z. Fu, J. Li, J. Ghosen, M. Zeng, J. Stebbins, P. N. Prasad and M. T. Swihart, *ACS Nano*, 2017, **11**, 6370–6381.
43 X. Liu, H. Jiang, J. Ye, C. Zhao, S. Gao, C. Wu, C. Li, J. Li and X. Wang, *Adv. Funct. Mater.*, 2016, **26**, 8694–8706.
44 M. Sakurai, T. Ueta and C. Joachim, *Adv. Electron. Mater.*, 2023, **9**, 2300347.